Sustainable Energy & Fuels

ROYAL SOCIETY OF CHEMISTRY

PAPER

View Article Online
View Journal

Cite this: DOI: 10.1039/d6se00103c

Nanocomposite electrodes with CuFe layered double hydroxides and hydrochar for alkaline HER and HOR: a multifunctional platform for hydrogen electrocatalysis

Michelle Saliba,[ab] Philippe Knauth, *[a] Emily Bloch,[a] Luca Pasquini,[a] Emanuela Sgreccia,[b] Riccardo Narducci, [b] Alessandra Varone[b] and Maria Luisa Di Vona *[b]

The hydrogen evolution reaction (HER) and hydrogen oxidation reaction (HOR) in alkaline media remain limited by slow kinetics and the reliance on noble metal catalysts. Copper-iron layered double hydroxides (CuFe-LDHs), composed of non-rare and low-toxicity elements, offer a sustainable alternative, though their performance is restricted by low conductivity and limited accessibility of active sites. In this work, CuFe-LDHs were synthesized hydrothermally and modified through three complementary strategies: ammonium fluoride (NH_4F) as a structure-directing agent poly(2,6-dimethyl-1,4-phenylene oxide) functionalized with trimethylammonium (PPO-LC) as a hydroxide-conducting ionomer, and a nitrogen-doped hydrochar derived from pine needles as an electron-conducting additive. Structural tuning with 1.5% NH_4F produced highly crystalline LDH-1.5 with increased exposure of catalytic centers, while PPO-LC enhanced OH^- transport and electrode integrity. Hydrochar contributed additional conductive domains, facilitating charge transfer and improving electrode architecture. The materials were characterized using BET surface area analysis, scanning electron microscopy with EDS element mapping, X-ray diffraction, and Fourier-transform infrared spectroscopy. All catalytic electrodes demonstrated a high electrochemically active surface area. The LDH-1.5/PPO-LC electrode delivered the best HER activity with an overpotential of −332 mV at −10 mA cm^{-2}. For the HOR, hydrochar-containing electrodes displayed reduced onset potential values: the LDH-1.5/PPO-LC/HC composite reached the lowest onset potential of 38 mV, though the current densities remained limited. Tafel analysis indicated that the HER is governed by the Volmer step associated with water dissociation, whereas the HOR follows a Heyrovsky–Volmer or Tafel–Volmer pathway depending on the electrode composition. These results highlight the effectiveness of combining structural, ionic, and electronic modifications to enhance the performance of CuFe-LDH-based bifunctional electrodes in alkaline environments, while indicating that further optimization is required to overcome intrinsic kinetic limitations.

Received 26th January 2026
Accepted 31st March 2026

DOI: 10.1039/d6se00103c

rsc.li/sustainable-energy

Introduction

Hydrogen is considered as a key energy vector in the transition toward sustainable and low-carbon energy systems. Its high gravimetric energy density, storability over long timescales, and ability to be used across diverse applications, ranging from transportation and industrial decarbonization to large-scale energy storage, make it an attractive carrier for a low-carbon economy.[1–3] Realizing this potential requires efficient and scalable routes for both hydrogen generation and utilization. Electrochemical technologies, such as water electrolysis and fuel cells, are among the most promising solutions; they rely on the hydrogen evolution reaction (HER) and hydrogen oxidation reaction (HOR), respectively. Alkaline systems offer several advantages over acidic environments, such as lower corrosion rates, reduced system costs, and compatibility with catalysts derived from earth-abundant elements. However, the kinetics of the HER and HOR under alkaline conditions are slow, with exchange current densities that can be up to two orders of magnitude lower than those achieved in acidic electrolytes.[4–6] This kinetic barrier raises energy losses and reduces the efficiency of hydrogen conversion. Consequently, the design of

[a]Aix Marseille Univ, CNRS, MADIREL (UMR 7246) and International Laboratory: Ionomer Materials for Energy, Campus St Jérôme, 13013 Marseille, France. E-mail: philippe.knauth@univ-amu.fr

[b]University of Rome Tor Vergata, Dep. Industrial Engineering and International Laboratory: Ionomer Materials for Energy, 00133 Roma, Italy. E-mail: divona@uniroma2.it

electrocatalysts that are both efficient and composed of abundant, non-noble elements is a central challenge for the advancement of hydrogen-based technologies.

Among the wide range of nanomaterials explored for clean energy conversion, layered double hydroxides (LDHs) have emerged as promising electrocatalysts for alkaline water splitting, owing to their tunable composition, hydroxide conductivity, high surface area, and favorable redox properties.[7–13] Their general formula, $[(M^{2+})_{1-x}(M^{3+})_x(OH)_2]^{x+}(A^{m-1})_{x/m}\cdot nH_2O$, describes a lamellar structure consisting of positively charged hydroxide layers with divalent (M^{2+}) and trivalent (M^{3+}) metal cations, whose charge is balanced by exchangeable interlayer anions. This brucite-derived architecture enables precise modulation of catalytic properties *via* targeted cation substitution. NiFe-LDH has long served as a benchmark system, due to the synergistic interaction between Ni^{2+} and Fe^{3+}, which enhances adsorption of reaction intermediates and improves the catalytic performance.[14] However, recent studies show that replacing Ni with Cu in LDH structures can further enhance catalytic activity. Furthermore, copper is generally considered "greener" than nickel due to its lower toxicity, wider abundance and lower cost, better recyclability, and moderate environmental impact when used in catalytic amounts. In LDH, Cu^{2+} contributes to electronic conductivity *via* its partially filled 3d orbitals, accelerating the Volmer step of the HER.[15] Simultaneously, Fe^{3+} facilitates electron delocalization, ensuring efficient charge transfer throughout the catalytic cycle.[15–17] Additionally, the presence of iron oxides, particularly Fe_2O_3, has been reported to enhance the hydrogen evolution kinetics by promoting water dissociation and optimizing hydrogen adsorption. This enhancement is attributed to strong electronic coupling with adjacent metal centers, which modulates the hydrogen binding free energy and lowers energy losses.[18,19] Although CuFe-LDHs have mainly been explored for the HER, their redox flexibility, intrinsic hydroxide conductivity, stability in alkaline media, and structural adaptability also make them strong candidates for the HOR, pointing to their potential as bifunctional electrocatalysts.

Despite these advantages, CuFe-based LDHs suffer from inherent drawbacks such as low electronic conductivity, limited crystallinity, and restricted access to active sites. Strategies to overcome these issues have included coupling with conductive scaffolds (*e.g.* CuFe-LDH on Ni foam or NiFe-LDH on a Cu_xO support) and introducing ternary compositions (*e.g.* CoCuFe-LDH on graphene) to enhance charge transport and exploit redox synergies.[20–22] More recently, attention has turned toward *in situ* structural engineering during synthesis using ammonium fluoride (NH_4F).[23] Acting as a mild etchant and coordinating agent, NH_4F promotes the formation of ultrathin, porous, and defect-rich nanosheets, thereby increasing the surface area, enhancing the electrolyte accessibility, and exposing more catalytically active edge sites.[23–25] Such morphological control has been shown to substantially improve electrochemical performance, as demonstrated for NiCo-LDHs that reach high specific capacitances while retaining stability over thousands of cycles.[26]

In this work, we investigated CuFe-LDH synthesized without a structure-directing agent and with two different concentrations of NH_4F added during the synthesis (1.5% and 4.5%). In parallel with structural tuning, ionic transport across the catalyst layer remains a critical factor for overall efficiency. Incorporating hydroxide-ion conducting ionomers such as poly(2,6-dimethyl-1,4-phenylene oxide) functionalized with trimethylammonium (PPO-LC) provides a means to improve OH^- conductivity. The long, flexible side chains of PPO-LC promote nanophase separation and hydrophilic network connectivity while also reinforcing mechanical integrity and adhesion, making it an effective additive for electrocatalytic systems.[27,28] Furthermore, growing attention has been directed toward the integration of biomass-derived carbon materials, particularly biochar, to further improve the electronic conductivity and electrocatalytic performance. Hydrochar (HC), produced from pine needles *via* hydrothermal carbonization in the presence of urea, offers a nitrogen-doped porous carbon matrix with moderate conductivity and abundant functional groups (–OH, –COOH, and $–NH_2$). These features improve the dispersion of active phases, facilitate charge transport, and enhance electrolyte penetration.[29] HC has already shown promise in reactions such as oxygen and carbon dioxide reduction, where hydrochar-based electrodes displayed favorable onset potentials and supported efficient multi-electron transfer processes.[30] Incorporating HC is a promising approach to improve electron mobility, stabilize the dispersion, and optimize the interfacial architecture within the catalytic layer, but its use in CuFe-LDH systems for the HER and HOR has not been explored.

The novelty of this work lies in the preparation of CuFe-LDH-based electrodes *via* a hydrothermal route, systematically combining NH_4F for structural optimization, PPO-LC for hydroxide conduction, and pine needle-derived hydrochar (HC) for electronic conduction and porous support. This design enables the evaluation of not only the individual effects of each additive but also their potential synergistic contributions to governing HER and HOR activity under alkaline conditions. Through this approach, the study aims to identify key structure–property relationships that can guide the development of efficient, low-cost, and sustainable electrocatalysts for hydrogen technologies.

Materials and methods

Materials

Semi-dried pine needles were collected from the vicinity of the University of Perugia, Italy. Urea (99%, carbamide, $CO(NH_2)_2$, Merck KGaA, Darmstadt, Germany) was used as the nitrogen precursor. All other reagents were used as received from Sigma-Aldrich, including copper(II) nitrate trihydrate ($Cu(NO_3)_2\cdot 3H_2O$, 99%), iron(III) nitrate nonahydrate ($Fe(NO_3)_3\cdot 9H_2O$, > 98%), *n*-butyllithium (BuLi, 2.5 M in hexane), trimethylamine (TMA, 31–35 wt% in ethanol, 4.2 M), and poly(2,6-dimethyl-1,4-phenylene oxide) (PPO, $M_W = 50\,000$ g mol^{-1}). Carbon paper (AvCarb EP55) was purchased from the Fuel Cell Store. Potassium hydroxide (KOH, 85%) used for electrochemical measurements was supplied by LabCAM.

Synthesis of CuFe-LDH

CuFe-LDH was synthesized by a hydrothermal method using $Cu(NO_3)_2 3H_2O$, $Fe(NO_3)_3 \cdot 9H_2O$, and urea as precursors. Aqueous solutions of Cu^{2+} (0.25 M) and Fe^{3+} (0.125 M) were mixed at a Cu : Fe molar ratio of 2 : 1 and stirred for 20 min. Different amounts of NH_4F (0, 1.5 mol%, or 4.5 mol% with respect to Cu^{2+}) were then introduced, followed by the addition of urea (molar ratio urea: Fe = 10 : 1). After stirring for 1 h, the suspension was transferred to a Teflon-lined autoclave and heated at 90 °C for 24 h. The precipitate was collected by centrifugation, washed with deionized water, and dried at 60 °C for 3 days.

Synthesis of hydrochar

Hydrochar was prepared as reported in ref. 31. In brief, 2 g of untreated pine needle waste was hydrothermally treated in 20 mL of deionized water (1 : 10 solid-to-liquid ratio) at 230 °C for 1 h. The product was filtered, washed with hot water until colorless, and dried under vacuum at 105 °C. The dried hydrochar was then mixed with melamine (1 : 1 wt ratio) and pyrolyzed at 800 °C for 1 h under an inert atmosphere to obtain N-doped hydrochar, which was stored in an airtight container until use. Elemental composition (wt%): C 75.2, N 10.5, H 1.0, O 4.1.

Synthesis of CuFe-LDH supported on hydrochar (CuFe-LDH/HC)

CuFe-LDH/HC was synthesized under the same conditions in the presence of hydrochar. Hydrochar (15 wt% relative to the total salt mass) was dispersed in deionized water by ultrasonication for 20 min prior to metal salt addition. Cu^{2+} and Fe^{3+} were introduced at a Cu : Fe molar ratio of 2 : 1 (0.25 M and 0.125 M, respectively), followed by NH_4F (1.5 mol% relative to Cu^{2+}) and, after 10 min, urea (urea:Fe = 10 : 1). The mixture was stirred for 1 h, hydrothermally treated at 90 °C for 24 h, centrifuged, washed, and dried at 60 °C for 3 days.

Synthesis of PPO-LC

The synthesis of PPO-LC was performed as described in ref. 32. Briefly, PPO (41.7 meq) was dissolved in THF (500 mL) and reacted with BuLi (62.6 mmol, 2.5 M in hexane) at 55 °C for 3 h. The reaction mixture was then cooled to −70 °C, followed by the addition of 1,4-dibromobutane (125 mmol). The mixture was stirred overnight at room temperature. The product was precipitated and washed with ethanol. Quaternization was carried out *via* nucleophilic substitution in *N*-methylpyrrolidone (NMP) using excess TMA. After heating at 80 °C for 72 h, the polymer was precipitated in water, filtered, washed, and vacuum-dried at 60 °C. The obtained ionomer, PPO-LC, exhibited a degree of amination of 0.38 and an IEC of 0.99 meq g^{-1}.

Catalyst ink and electrode preparation

Catalyst inks were prepared by dispersing 40 mg of hydrothermally obtained powder (LDH, LDH-NH_4F, or LDH-NH_4F-HC), with or without 10 mg PPO-LC, in dimethyl sulfoxide (DMSO). The suspensions were stirred at room temperature and sonicated overnight. A 5 μL aliquot of ink was drop-cast onto acid-treated carbon paper (pretreated according to ref. 33) and dried under vacuum at 40 °C for 4 h. The final catalyst loading was (0.23 ± 0.03) mg per electrode. The electrodes were fixed to glassy carbon disks with 6 mm diameter for electrochemical testing. The electrode compositions are reported in Table 1.

Table 1 Composition and formulation codes of the synthesized CuFe-LDH-based electrodes

Electrode code	NH_4F	Ionomer	Hydrochar (HC)
LDH/PPO-LC	—	PPO-LC	—
LDH-1.5/PPO-LC	1.5	PPO-LC	—
LDH-4.5/PPO-LC	4.5	PPO-LC	—
LDH/HC	—	—	230_1800_1
LDH-1.5/HC	1.5	—	230_1800_1
LDH-1.5/PPO-LC/HC	1.5	PPO-LC	230_1800_1

Characterization

The electrode morphology was investigated by scanning electron microscopy (ZEISS Gemini SEM 500), coupled with an EDAX Octane Silicon Drift Detector for elemental mapping (EDS).

XRD patterns were collected using Cu-Kα radiation (λ = 0.1508 nm), in step-scanning mode with a 2θ step of 0.05° and counting time per step of 5 s. Phase identification was performed by comparing the experimental pattern with the JCPDS-ICDD database.

Fourier Transform Infrared (FTIR) spectra were obtained using a PerkinElmer Spectrum 2 IR spectrometer equipped with an ATR ZnSe crystal.

The N_2 adsorption–desorption isotherms were measured at 77 K on a BelSorp MAX from BelJapan. The specific surface area was determined by the Brunauer, Emmett and Teller (BET) method and the pore volume using the t-plot.[34] Prior to adsorption, the samples were outgassed at 250 °C overnight under vacuum using the BelPrep apparatus.

Electrochemical measurements

Electrochemical measurements were performed in a conventional H-cell, using a three-electrode configuration. The setup consisted of a rotating disk electrode (RDE, 0.28 cm^2, OrigaTrod, OrigaLys) as the working electrode, platinum foil (4 cm^2) as the counter electrode, and an Ag/AgCl reference electrode positioned close to the working electrode. All experiments were carried out in 1 M KOH at room temperature for both the HER and the HOR. A BioLogic VMP3 potentiostat was employed to perform cyclic voltammetry (CV), linear sweep voltammetry (LSV), chronopotentiometry (CP), and electrochemical impedance spectroscopy (EIS). CV curves were recorded at scan rates ranging from 20 to 100 mV s^{-1}, while EIS spectra were collected in the frequency range of 1 MHz to 1 Hz with a perturbation amplitude of 20 mV. LSV measurements were conducted at a scan rate of 5 mV s^{-1} with electrode rotation at 1000 rpm to

remove hydrogen bubbles during the HER and to enhance mass transport during the HOR. All measured potentials were converted to the reversible hydrogen electrode (RHE) scale using the equation: $E_{RHE}/V = E_{Ag/AgCl} + 0.059\ pH + 0.197$ and ohmic drop correction was applied.

Results and discussion

CuFe-LDH was synthesized hydrothermally using $Cu(NO_3)_2$, $Fe(NO_3)_3$, and urea. In the absence of NH_4F, the slow release of OH^- from urea hydrolysis promoted LDH precipitation with carbonate anions from solution or atmospheric CO_2 occupying the interlayer. However, the resulting material displayed relatively broad and low intensity diffraction peaks, suggesting poor crystallinity and possible coexistence of amorphous hydroxide phases. When NH_4F was introduced as an additional mineralizer, fluoride ions could interact with Cu^{2+} and Fe^{3+} during nucleation, modifying the growth mechanism. The mechanism of F^- regulation is illustrated in ref. 35. At a molar ratio of NH_4F: Cu = 0.015 (LDH-1.5), the XRD pattern (Fig. 1a) exhibited sharper and more intense reflections, indicating improved crystallinity. This enhancement can be attributed to the ability of F^- to stabilize metal hydroxide layers and regulate crystal growth, leading to larger and more ordered LDH domains. In contrast, at higher NH_4F content (NH_4F : Cu = 0.045, LDH-4.5), less intense diffraction peaks and reduced phase purity were observed. The XRD pattern of LDH-1.5 confirms the formation of the LDH phase. The characteristic LDH reflections corresponding to the (003), (006), (012), and (015) planes are observed at 11.9°, 24.2°, 32.3°, and 37.1°, respectively. Additional diffraction peaks are detected and attributed to Fe_2O_3 (ICDD PDF 40-1139) and FeOOH (ICDD PDF 08-0098), indicating the presence of minor secondary phases.

As shown in Fig. 1a, the experimental diffraction pattern is compared with the standard pattern of LDH (ICDD PDF card No. 41-1428) and the positions of the main reflections are in good agreement with the reference one, confirming the formation of the LDH structure. A slight shift of the experimental diffraction peaks is observed, which may indicate variations according to Bragg's law; the lattice parameters of the LDH structure were calculated and the values $a = 0.33$ nm and $c = 2.22$ nm are consistent with those reported for Fe–Cu LDH systems.[24]

To further investigate the chemical structure and functional groups of the composite material, FTIR analysis was performed. The FTIR spectrum of CuFe-LDH grown on hydrochar (CuFe-LDH/HC) is compared with that of pristine hydrochar in Fig. 1b. A broad absorption band centred around 3400 cm^{-1} is especially prominent in the CuFe-LDH/HC sample, and is attributed to O–H stretching vibrations from both interlayer water and hydroxide ions within the LDH layers. The corresponding H–O–H bending vibration of interlayer water appears at 1670 cm^{-1}, where it overlaps with the C=O stretching bands from carboxyl or carbonyl groups in the hydrochar matrix.[36] A sharp peak near 3770 cm^{-1} is observed and can be assigned to isolated O–H stretching vibrations, which may arise from non-hydrogen-bonded terminal OH groups on LDH crystallites, or from coexisting phases such as Fe_2O_3. In the lower wavenumber region, bands at 535 cm^{-1} and 678 cm^{-1} correspond to Cu–O and Fe–O vibrational modes, respectively.[36,37] A feature at 942 cm^{-1} may be attributed to M–O–H bending vibrations, consistent with the layered hydroxide structure.[24] Notably, the CuFe-LDH/HC spectrum exhibits a strong absorption band at about 1500 cm^{-1} and a weaker one near 860 cm^{-1}, both characteristic of the carbonate anion (CO_3^{2-}). This confirms that carbonate is the predominant interlayer anion, likely incorporated from atmospheric CO_2 during synthesis, which employed urea hydrolysis under controlled pH conditions. Additionally, a distinct band at 1265 cm^{-1} is observed, which may result from interactions between the LDH layers and the aromatic moieties of the hydrochar surface.

To complement the structural characterization, the textural properties of the carbon support were investigated. The adsorption/desorption isotherm of hydrochar (Fig. 1c) shows clearly the existence of micropores (type I isotherm). The BET surface area is 353 $m^2\ g^{-1}$ and the pore volume is 0.14 $cm^3\ g^{-1}$. A high temperature heat treatment of hydrochars is known to increase significantly their surface area.[38]

Representative SEM images (Fig. 2) of (a) LDH-1.5/PPO-LC and (b) LDH-1.5/PPO-LC/HC on carbon paper show fibers

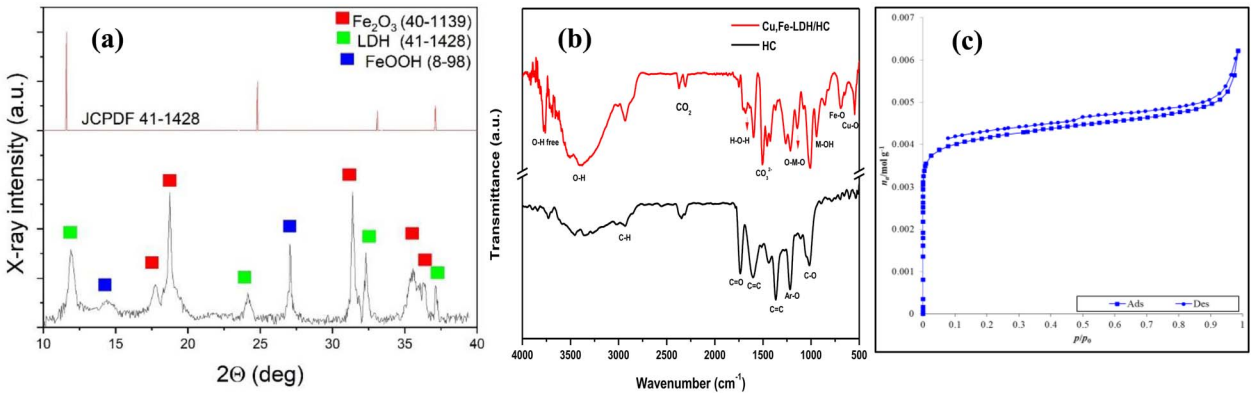

Fig. 1 Structural and textural characterization of LDH-based materials: (a) X-ray diffraction pattern of LDH-1.5, (b) FTIR spectra of hydrochar (HC) and CuFe-LDH/HC composite, and (c) N_2 adsorption–desorption isotherm of hydrochar at 77 K.

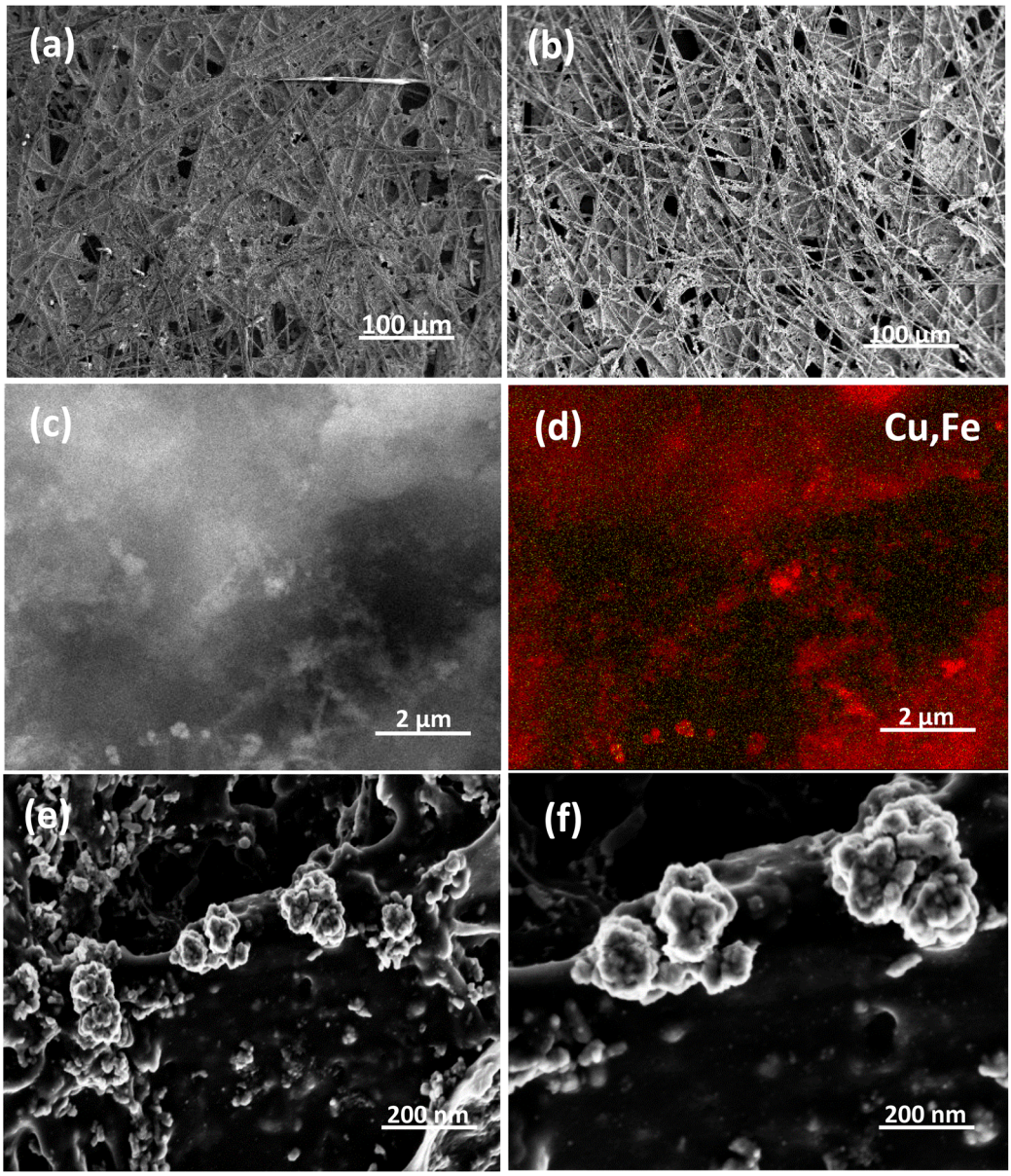

Fig. 2 SEM micrographs of representative electrode microstructures: (a) LDH-1.5/PPO-LC, (b) LDH-1.5/PPO-LC/HC, (c) higher magnification SEM image with (d) corresponding EDS elemental mapping (red Fe and yellow Cu) of LDH-1.5/PPO-LC, and (e and f) further magnified SEM images highlighting the LDH domains.

uniformly coated with thin LDH/PPO-LC films. In sample (a), the coating appears smoother with smaller porous domains and only a few larger openings. With hydrochar (b), the structure becomes more heterogeneous, showing both small and larger interconnected pores. The addition of HC therefore increases surface heterogeneity and pore variety while preserving the fiber scaffold. The spatial distribution of elements in the LDH-1.5/PPO-LC electrode was further examined by EDS mapping on a high-resolution SEM image (Fig. 2c). The elemental maps of Fe and Cu revealed a uniform distribution of both metals across the surface, while a zoomed-in view of the brightest regions (Fig. 2d) highlighted LDH domains, confirming the successful formation of the CuFe-LDH phase (Fig. 2e and f). The higher Fe intensity is attributed to the presence of iron oxides, as confirmed by XRD. Such homogeneous dispersion of active components within the three-dimensional electrode framework is expected to increase the density of accessible active sites, thereby facilitating the adsorption–desorption processes during the HER and HOR.[39] The corresponding EDS results for LDH-1.5/PPO-LC/HC show similar elemental distributions.

The electrochemically active surface area (ECSA) is a fundamental parameter that reflects the density of catalytically accessible sites. To obtain the ECSA, the double-layer capacitance (C_{dl}) must first be determined, and in this work, it was evaluated using two complementary electrochemical methods. The first approach was electrochemical impedance

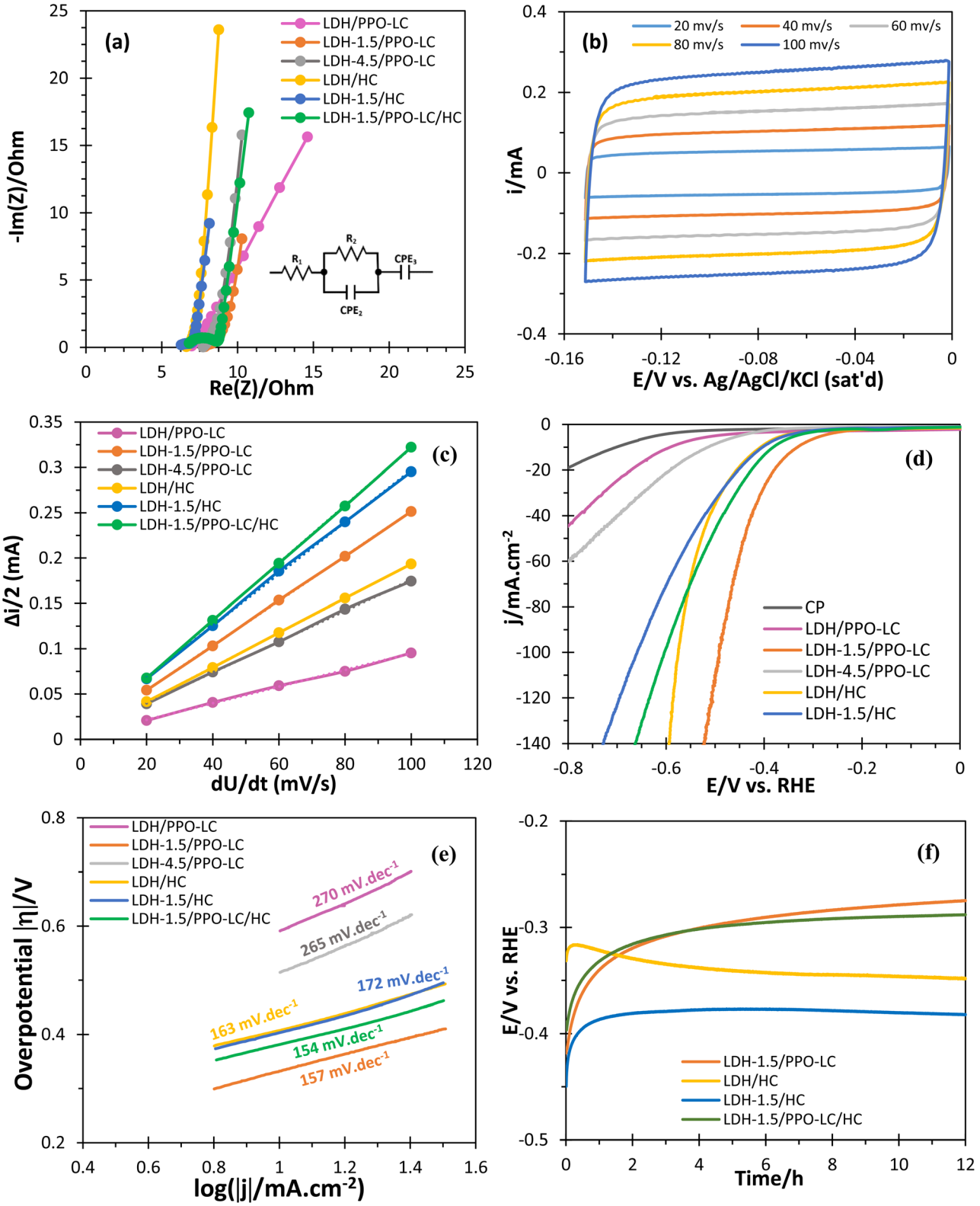

Fig. 3 Electrochemical characterization and HER performance of electrodes with different compositions in 1 M KOH: (a) electrochemical impedance spectroscopy (EIS) Nyquist plots, (b) cyclic voltammograms of LDH-1.5/PPO-LC at various scan rates, (c) double-layer capacitance (C_{dl}) of the electrodes, (d) linear sweep voltammograms (5 mV s^{-1}) for the hydrogen evolution reaction at 1000 rpm in H_2-saturated 1 M KOH, (e) corresponding Tafel plots, and (f) chronopotentiometric stability test at −10 mA cm^{-2} and 1000 rpm.

Table 2 Electrochemical properties from CV, EIS and LSV for various CuFe-LDH-based electrodes in 1 M KOH

Electrode	C_{dl} (mF)	ESCA (cm^2)	R_1 (Ω)	R_2 (Ω)	Q_2 (mF s^{n-1})	n_2	Q_3 (mF s^{n-1})	n_3	Overpotential (mV)/HER @ −10 mA cm^{-2}	E_{onset} (mV)/HOR
LDH/PPO-LC	0.9	30	6	1.4	—	—	1.1	0.7	−592	—
LDH-1.5/PPO-LC	2.4	80	7.7	1.7	19	0.45	2.9	0.91	−332	80
LDH-4.5/PPO-LC	1.7	57	7.7	1.4	16.5	0.58	1.8	0.94	−513	—
LDH/HC	1.9	63	6.6	1.1	56	0.46	2.4	0.97	−407	70
LDH-1.5/HC	2.8	93	6	1.2	3.6	0.53	3.3	0.93	−403	60
LDH-1.5/PPO-LC/HC	3.2	107	6.9	1.7	0.3	0.71	3.4	0.93	−381	38

spectroscopy (EIS). Nyquist plots (Fig. 3a) were fitted using the equivalent circuit R_1−(R_2‖CPE_2)−CPE_3, where R_1 represents the electrolyte–electrode resistance, R_2 the charge-transfer resistance, CPE_2 accounts for interfacial processes, and CPE_3 corresponds to the electrode capacitance. The intercept on the real axis yielded similar R_1values for all electrodes (average 6.8 Ω; Table 2), indicating comparable ohmic resistance. The impedance of a constant phase element is given by the following relation:

$$Z = [Q(i\omega)^n]^{-1} \quad (1)$$

where i is the imaginary unit and ω is the angular frequency. Exponents of $n \approx 0.5$ indicate diffusion-limited (Warburg-type) behavior, whereas $n \approx 1$ reflects ideal capacitive behavior.[40,41] Here, the CPE_3 exponents were close to unity, supporting their assignment to electrode capacitances, while the CPE_2 exponents indicate diffusion limitations.

A second, independent determination of C_{dl} was obtained from cyclic voltammetry (CV) performed in the non-faradaic region, where the voltammograms exhibit the characteristic rectangular shape of double-layer charging (Fig. 3b). The capacitive current ($\Delta i/2$) was plotted as a function of scan rate (Fig. 3c), and the slope of the linear fit yielded C_{dl} according to the following relation:

$$\frac{\Delta i}{2} = C_{dl}\left(\frac{dE}{dt}\right) \quad (2)$$

The C_{dl} values obtained from CV showed excellent agreement with those extracted from EIS ($C_{dl} \approx CPE_3$), confirming the reliability of the capacitance determination.

The ECSA was calculated using the following equation:

$$\mathrm{ECSA} = \frac{C_{dl}}{C_s} \quad (3)$$

where C_s is the specific capacitance; a value of 30 μF cm^{-2} was adopted, consistent with previous reports for LDH-based materials.[41,42] All extracted values are summarized in Table 2.

A clear trend was observed in the calculated ECSA values among the different electrodes. The LDH/PPO-LC electrode showed the lowest ECSA of 30 cm^2, consistent with a compact structure due to polymer blocking of active sites, as previously reported.[43–45] Incorporation of highly crystalline LDH-1.5 increased the ECSA to 80 cm^2, demonstrating the role of fluoride as a structure-directing agent that etches layers, generates edge sites, and achieves a favorable balance between defect creation and structural stability. Similar behavior has been reported for NiFe- and CoFe-LDHs, where fluoride facilitated the formation of ultrathin nanosheets with enhanced defect density and edge exposure, thereby boosting ECSA and catalytic activity.[23,46] However, increasing the NH_4F concentration to 4.5% during synthesis resulted in a lower ECSA of 57 cm^2, reflecting the detrimental effect of excessive fluoride, which induces lattice disorder.[47] Hydrochar provided an additional enhancement: when incorporated alone (LDH/Hydrochar), it increased the ESCA to 63 cm^2. Owing to its sp^2-carbon network and intrinsic porous structure, hydrochar forms a conductive framework that improves electron transport and electrolyte accessibility.[48–50] The LDH-1.5/PPO-LC/HC composite achieved the highest ESCA (107 cm^2), reflecting the synergistic interplay between NH_4F-induced defect generation and hydrochar. This combination maximized the density of accessible sites and improved charge-storage capacity, consistent with reports showing that LDHs modified by anion exchange, fluoride-assisted synthesis, or integration with biomass-derived carbons exhibit enhanced capacitances and faster kinetics compared to their unmodified counterparts[26,51,52].

The catalytic activity toward the hydrogen evolution reaction (HER) was subsequently evaluated by linear sweep voltammetry. The HER polarization curves (Fig. 3d) confirmed the trends inferred from the capacitance analysis. The LDH/PPO-LC electrode exhibited the lowest catalytic activity, requiring −592 mV to reach −10 mA cm^{-2}. In contrast, LDH-1.5/PPO-LC achieved a significantly lower overpotential of −332 mV, while LDH-4.5/PPO-LC gave an intermediate value (−513 mV), in line with the structural disorder discussed in the ECSA section. These results highlight the importance of optimizing the NH_4F concentration and demonstrate that HER performance is governed by surface structuring and ordering of LDH: when optimized, NH_4F expands the accessible area and facilitates charge/mass transport, whereas when excessive or poorly controlled, it induces lattice disorder and reduces activity.

Electrodes containing hydrochar displayed intermediate activity, with LDH/HC and LDH-1.5/HC requiring overpotentials of −407 and −403 mV, respectively. This suggests that hydrochar plays a non-negligible role by providing electronic conductivity and facilitating electron transfer. However, in

Table 3 Comparison of HER performance of LDH-based electrocatalysts reported in the literature and in this work

Catalyst	Overpotential (mV)	Support	Electrolyte	Reference
CuFe-LDH/Ni	−159	Ni foam	1M NaOH	15
Mo-doped CoFe-LDH	−192	Ni foam	1M KOH	53
Ni-doped-Co LDH	−104	Ni foam	1M KOH	54
Ce-doped NiFe-LDH	−147	Ni foam	1M KOH	55
LDH-1.5/PPO-LC	−332	Carbon paper	1M KOH	This work

systems with HC but without PPO-LC, ionic conduction occurs mainly through OH^- transport within the LDH layers, which is less efficient than ionomer-assisted conduction. Consequently, the best performance was obtained when highly crystalline LDH was combined with the ionomer binder: LDH-1.5/PPO-LC reached the lowest overpotential (−332 mV), followed closely by LDH-1.5/PPO-LC/HC (−381 mV).

Some LDH-based catalysts reported in the literature exhibit lower overpotentials, as summarized in Table 3. However, these performances were obtained on highly conductive and catalytically active supports such as Ni foam or by introducing less common or even toxic metals such as Co. In contrast, our electrodes were prepared on carbon paper *via* a simple hydrothermal process, relying on the intrinsic catalytic properties of CuFe-LDH without additional metals. Overall, these results demonstrate that a sustainable strategy, combining optimized crystallinity with ion and electron conducting pathways, can deliver competitive HER activity without relying on scarce or environmentally harmful elements. This approach provides a viable direction for designing eco-friendly electrocatalysts that balance performance and sustainability; however, further optimization is required to fully close the gap with state-of-the-art catalysts.

To further evaluate the intrinsic catalytic efficiency of the electrodes, the hydrogen generation rate (r_{H_2}) and the mass activity (MA) were calculated. The hydrogen production rate was determined according to the following equation:

$$r_{H_2,geo} = \frac{|I|}{2F \cdot A_{geo}} \quad (4)$$

where $|I|$ is the absolute value of the measured current (A), F is the Faraday constant (96 485 C mol^{-1}), and $A_{geo}$is the geometric electrode area (0.28 cm^2). The factor of 2 accounts for the two electrons required for the formation of one molecule of H_2. A faradaic efficiency of 100% was assumed for the calculation.

The mass activity was calculated as follows:

$$MA = \frac{|j|}{m} \quad (5)$$

where j is the current density (mA cm^{-2}) at a given potential and m is the catalyst loading (mg cm^{-2}). Both the hydrogen production rate and the mass activity were evaluated over the potential range from −0.1 to −0.5 V. For all electrodes, the hydrogen production rate increases as the applied potential shifts to more negative values, as evidenced by the corresponding increase in $r(H_2)$ (Fig. 4a). To enable a direct comparison between the catalysts, a three-dimensional representation of the MA at −0.4 V was generated (Fig. 4b), reflecting the same trends observed across the entire potential range. Among the investigated materials, LDH-1.5/PPO-LC exhibits the highest hydrogen production rate ($r(H_2) = 0.52$ mmol h^{-1} cm^{-2}) and mass activity (34 mA mg^{-1}) at −400 mV and retains the highest values at other applied potentials, highlighting the beneficial effect of the optimized LDH composition. The high

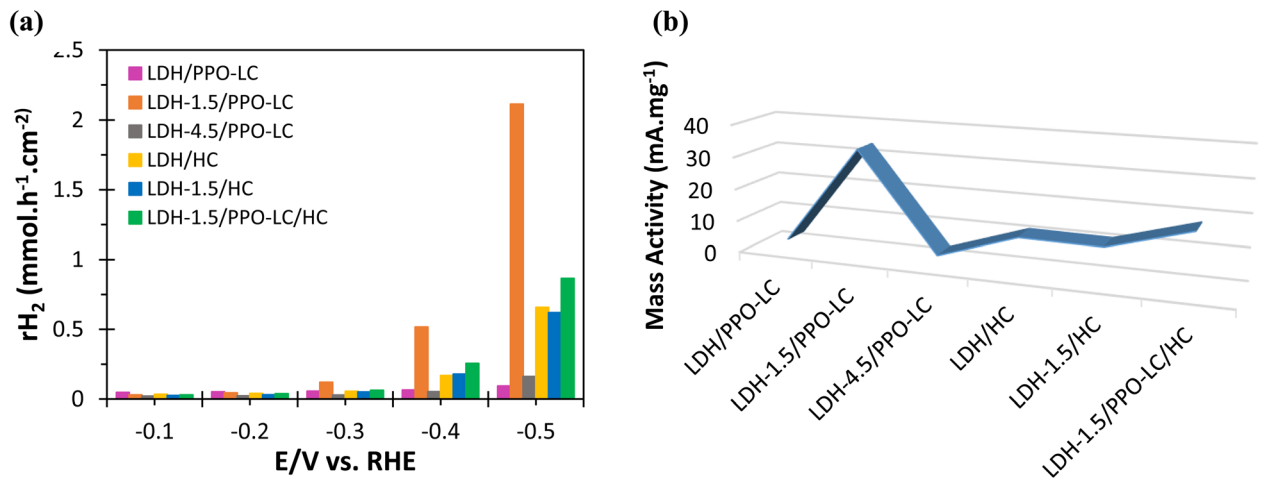

Fig. 4 Intrinsic catalytic activity of CuFe-LDH-based electrodes toward the hydrogen evolution reaction in alkaline medium: (a) hydrogen generation rate (r_{H_2}) as a function of the applied potential (*E vs.* RHE) and (b) mass activity (MA) at −0.4 V.

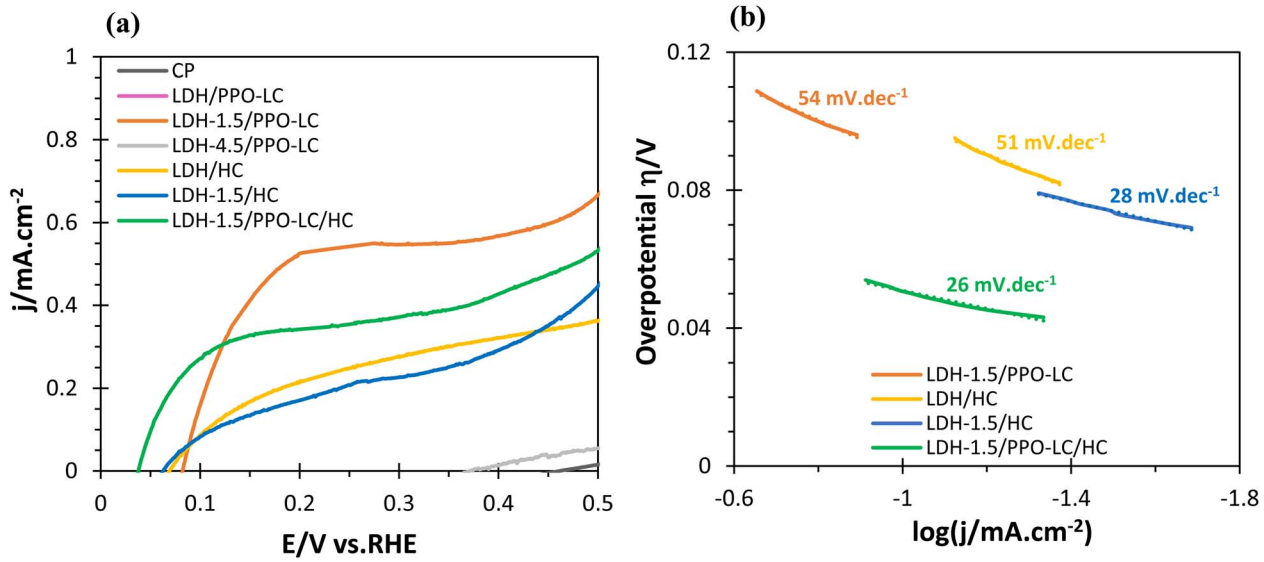

Fig. 5 HOR activity of electrodes with different compositions in 1 M KOH: (a) linear sweep voltammograms (5 mV s^{-1}, 1000 rpm) recorded in H_2-saturated electrolyte and (b) corresponding Tafel slopes.

production rates with incorporation of HC indicate that the carbon phase positively contributes to the overall catalytic behaviour, with LDH-1.5/PPO-LC/HC displaying the second-highest activity.

To gain further insight into the reaction kinetics governing the HER process, the Tafel slopes were extracted from the LSV curves (Fig. 3e). The electrodes with low crystallinity LDH exhibit higher Tafel slopes, whereas the incorporation of LDH-1.5 and HC decreases the slope through improved charge transfer. Despite these improvements, all slopes remain above 120 mV dec^{-1}, highlighting the intrinsic kinetic limitations of LDH catalysts in alkaline HER. In alkaline electrolytes, the HER typically proceeds through an initial Volmer step involving water dissociation, generally associated with a Tafel slope of ~120 mV dec^{-1}:

$$H_2O + e^- + * \rightarrow H^* + OH^- \quad (6)$$

This step can be followed by either the Tafel recombination step (characterized by a Tafel slope of ~30 mV dec^{-1}):

$$H^* + H^* \rightarrow H_2 \quad (7)$$

or the Heyrovsky electrochemical desorption step, typically associated with a Tafel slope of ~40 mV dec^{-1}:

$$H_2O + e^- + H^* \rightarrow H_2 + OH^- \quad (8)$$

where * denotes an active catalytic site and H* represents adsorbed hydrogen atoms.[56–58] In both pathways, the reaction initiates with the adsorption of water molecules on the catalytic surface, followed by their dissociation and reduction into adsorbed hydrogen atoms and hydroxide ions. The hydroxide ions subsequently desorb into the electrolyte, regenerating the active sites and enabling the evolution of molecular hydrogen. This process is accelerated by the hydroxide-conducting ionomer.

In the present work, the Tafel slopes (Fig. 3e) indicate that the rate-determining step (RDS) of the HER is the Volmer reaction, which involves water dissociation. This behavior is attributed to the intrinsic kinetic barrier associated with H–OH bond cleavage and is consistent with previous reports on HER kinetics in alkaline media[8,57,58].

Finally, chronopotentiometric tests (Fig. 3f) demonstrated good stability for all four active electrodes, including the hydrochar-containing variant. A decrease in overpotential after 12 h at −10 mA cm^{-2} was observed for electrodes containing LDH-1.5, consistent with a better availability of active sites, whereas the overpotential increased for the less crystalline LDH samples, indicating their lower stability in alkaline medium.

Linear sweep voltammograms for the HOR are presented in Fig. 5a. The onset potential (E_{onset}, Table 2) decreased from 80 mV for LDH-1.5/PPO-LC to 70 mV with LDH/HC, 60 mV with LDH-1.5/HC, and 38 mV for the LDH-1.5/PPO-LC/HC electrode. In contrast, electrodes containing poorly crystalline LDH and no HC (LDH/PPO-LC and LDH-4.5/PPO-LC) showed negligible HOR activity. Importantly, hydrochar-containing electrodes exhibited the lowest onset potentials, suggesting the direct involvement of HC in the catalytic process. The very low value of 38 mV obtained with the optimized formulation reflects the synergistic effects of NH_4F improving crystallinity, HC providing supplementary catalytic sites and an electronically conductive framework, and the PPO-LC ionomer enhancing hydroxide transport. These combined factors increase the electrocatalytic activity at the electrode–electrolyte interface, enabling the HOR to initiate more easily.

However, although hydrochar lowers the onset potential, the corresponding current densities are smaller than those of the electrodes without it, suggesting that its presence partially

blocks some hydrogen diffusion pathways. In all cases, the current density did not exceed 1 mA cm^{-2}, with the highest value ($\sim$0.6 mA cm^{-2}) achieved by LDH-1.5/PPO-LC. The main limitation is related to mass-transport effects in alkaline media, where hydrogen solubility and diffusion are low, and even the most active catalysts typically reach only a few mA cm^{-2} under rotating-disk conditions.[59–63] This underscores the need for further electrode engineering to improve hydrogen delivery and utilization in order to translate the improved onset potentials into higher practical HOR currents in alkaline fuel cells.

The Tafel slope analysis for the HOR (Fig. 5b) further supports the LSV results. The four best-performing electrodes, particularly those incorporating hydrochar (HC), exhibit faster kinetics for the HOR than for the HER. LDH-1.5/PPO-LC and LDH/HC show Tafel slopes of approximately 50 mV dec^{-1}, values typically associated with a Heyrovsky–Volmer regime in which the RDS involves the reaction between adsorbed hydrogen species and OH^-. When the highly crystalline LDH-1.5 phase is combined with HC, the slope decreases markedly to 26 mV dec^{-1} for LDH-1.5/PPO-LC/HC, a value among the lowest reported for non-noble metal HOR catalysts.[64] According to established microkinetic analyses of the reversible hydrogen reaction,[56,57] slopes close to $\sim$30 mV dec^{-1} are generally attributed to a Tafel–Volmer pathway, indicating that the dissociation of adsorbed hydrogen gas becomes the rate-determining step.

If we compare the HER and HOR results, the role of hydrochar differs between these two reactions. Although the incorporation of HC improves the HOR onset potential and kinetics and increases the capacitive response, this effect does not translate into improved HER activity. This difference arises from the distinct rate-determining steps of the two reactions. The HOR mainly requires efficient hydrogen oxidation and rapid electron transfer from the catalytic sites to the electrode, which is facilitated by the conductive carbon framework of hydrochar. In contrast, the HER in alkaline media is limited by the water dissociation step, which requires highly active catalytic sites capable of breaking the O–H bond. Since hydrochar does not significantly promote this step and may partially cover the active LDH surface, its contribution to the HER remains limited. Consequently, hydrochar mainly improves electrode conductivity and structure, favoring HOR kinetics, while HER activity remains largely governed by the intrinsic LDH catalytic sites.

Conclusions

Layered Double Hydroxides (LDHs) are versatile materials for a wide range of applications, and CuFe-LDH, based on abundant and non-toxic elements, represents an appealing alternative to LDHs containing less benign and more rare metals, such as Co or Ni. In this study, we reported the preparation of six different CuFe-LDH-based electrodes and demonstrated that their electrocatalytic response is strongly governed by composition and structural features. The presence of an optimal concentration of 1.5% NH_4F as a structure-directing agent during hydrothermal synthesis enhanced crystallinity and increased the electrochemically active surface area (ECSA), while hydrochar boosted the ECSA through conductive networks and hierarchical porosity. The incorporation of a long-side-chain ionomer (PPO-LC) further improved the electrocatalytic performance.

The most crystalline ionomer-containing electrode (LDH-1.5/PPO-LC) delivered a HER current of -10 mA cm^{-2} at an overpotential of -332 mV and retained excellent stability, whereas its hydrochar analogue achieved comparable activity. In contrast, less crystalline LDH samples showed consistently lower performance.

For the HOR, LDH-1.5/PPO-LC reached the highest current density (0.6 mA cm^{-2}), while all hydrochar-containing electrodes exhibited lower onset potentials, with the most significant reduction to 38 mV observed for LDH-1.5/PPO-LC/HC, highlighting the role of hydrochar in improving electrocatalytic activity for hydrogen oxidation.

These results are consistent with the kinetic insights derived from the Tafel analysis. For the HER, the large slopes (>120 mV dec^{-1}) indicate that the reaction is limited by the Volmer step involving water dissociation. In contrast, the Tafel slopes for the HOR are consistent with a Heyrovsky–Volmer pathway for LDH-1.5/PPO-LC and LDH/HC, while the lower slope ($\sim$26 mV dec^{-1}) observed for LDH-1.5/PPO-LC/HC suggests a shift toward a Tafel–Volmer mechanism, reflecting faster hydrogen adsorption and improved HOR kinetics.

Overall, further optimization is required to overcome the intrinsic kinetic limitations of the HER, especially the water dissociation step, and the mass-transport barriers for the HOR, thereby enabling the development of more efficient bifunctional CuFe-LDH-based electrocatalysts for alkaline hydrogen technologies *via* a sustainable, scalable, and cost-effective route.

Conflicts of interest

There are no conflicts to declare.

Data availability

The supporting data have been provided as figures and tables in the main manuscript and as part of the supplementary information (SI). Supplementary information is available. See DOI: https://doi.org/10.1039/d6se00103c.

Acknowledgements

M. S., P. K. and L. P. gratefully acknowledge support from the French government under the France 2030 investment plan, as part of the Initiative d'Excellence d'Aix-Marseille Université – A*MIDEX project "ION-MEET", AMX-22-IN1-41.

References

1 J. Gómez and R. Castro, Green Hydrogen Energy Systems: A Review on Their Contribution to a Renewable Energy System, *Energies*, 2024, **17**(13), 3110.
2 M. G. Rasul, M. A. Hazrat, M. A. Sattar, M. I. Jahirul and M. J. Shearer, The Future of Hydrogen: Challenges on

Production, Storage and Applications, *Energy Convers. Manage.*, 2022, **272**, 116326.
3 T. Terlouw, L. Rosa, C. Bauer and R. McKenna, Future Hydrogen Economies Imply Environmental Trade-Offs and a Supply-Demand Mismatch, *Nat. Commun.*, 2024, **15**(1), 7043.
4 X. Mu, S. Liu, L. Chen and S. Mu, Alkaline Hydrogen Oxidation Reaction Catalysts: Insight into Catalytic Mechanisms, Classification, Activity Regulation and Challenges, *Small Struct.*, 2023, **4**(4), 2200281, DOI: 10.1002/sstr.202200281.
5 M. D. Woodroof, J. A. Wittkopf, S. Gu and Y. S. Yan, Exchange Current Density of the Hydrogen Oxidation Reaction on Pt/C in Polymer Solid Base Electrolyte, *Electrochem. Commun.*, 2015, **61**, 57–60.
6 J. Zheng, W. Sheng, Z. Zhuang, B. Xu and Y. Yan, Universal Dependence of Hydrogen Oxidation and Evolution Reaction Activity of Platinum-Group Metals on pH and Hydrogen Binding Energy, *Sci. Adv.*, 2016, **2**(3), e1501602, DOI: 10.1126/sciadv.1501602.
7 S. Nagappan, S. Yang, A. Adhikari, R. Patel and S. Kundu, A Review on Consequences of Flexible Layered Double Hydroxide-Based Electrodes: Fabrication and Water Splitting Application, *Sustain. Energy Fuels*, 2023, **7**(16), 3741–3775.
8 A. M. Tucker-Quiñónez, B. F. Rivadeneira-Mendoza, M. L. Gorozabel-Mendoza, I. B. Pérez-Almeida, A. J. García-Guerrero, A. A. Dueñas-Rivadeneira, K. K. Yadav, L. A. Zambrano-Intriago and J. M. Rodríguez-Díaz, Challenges and Potential of Layered Double Hydroxides as Electrocatalytic Materials for Hydrogen Production from Water: A Review of Recent Advances and Applications, *Energy Nexus*, 2025, 100399.
9 J. Chen, Y. Wu, H. Zheng, M. Chen, H. Sun, T. Zhou, G. Na, D. Li, Q. Lu and B. Zi, Facile Room-Temperature Synthesis of Pt/NiCo LDH for Enhanced Hydrogen Evolution Reaction, *Int. J. Hydrogen Energy*, 2024, **72**, 41–48.
10 Y. Zhang, Z. Zhang, X. Zhang, J. Li and R. Guo, Research Progress on NiCo-LDH Electrocatalysts for Oxygen Evolution Reaction, *Int. J. Hydrogen Energy*, 2025, **102**, 304–320.
11 M. Chettri, N. Diyali and B. Biswas, Tracking in situ transformation of metal–organic frameworks into layered double hydroxides during synthesis and alkaline water oxidation through operando mechanistic studies, *Dalton Trans.*, 2026, **55**(4), 1548–1583.
12 M. Tayebi, *et al.*, Production of H2 and glucaric acid using electrocatalyst glucose oxidation by the Ta NiFe LDH electrode, *ACS Appl. Mater. Interfaces*, 2024, **16**(20), 26107–26120.
13 Y. Shajirati, *et al.*, Facile synthesis of interlaced flower-like layered double hydroxides grown on porous CoMoP as a highly efficient electrocatalyst for hydrogen evolution reaction, *Energy*, 2023, **278**, 127840.
14 R. Xu, X. Wang, Z. Yang, Y. Chang, X. Chen, J. Wang and H. Li, Electrodeposition Fabrication of La-Doped NiFe Layered Double Hydroxide to Improve Conductivity for Efficient Overall Water Splitting, *ACS Appl. Energy Mater.*, 2024, **7**(9), 3866–3875, DOI: 10.1021/acsaem.4c00246.
15 M. Bhavanari, K.-R. Lee, C.-J. Tseng, I.-H. Tang and H.-H. Chen, CuFe Electrocatalyst for Hydrogen Evolution Reaction in Alkaline Electrolysis, *Int. J. Hydrogen Energy*, 2021, **46**(72), 35886–35895.
16 X. Li, S. Xu, J. Li, S. Zhang, B. Zhang, R. Zhao, D. Zhao and F. Wu, NiFe-LDH as a Bifunctional Electrocatalyst for Efficient Water and Seawater Electrolysis: Enhanced Oxygen Evolution and Hydrogen Evolution Reactions, *Nanoscale Adv.*, 2025, **7**, 5546–5560.
17 Y. Zhuang, S. Meng, Y. Wu, J. Li, X. Yang, C. Yuan, T. Peng and D. Guo, Enhanced Overall Water Splitting Performance in Alkaline Solutions Using Hollow Nanocage Nickel-Cobalt-Iron Layered Double Hydroxide Derived from Zeolitic Imidazolate Framework-67: The Synergy of Fast Etching and Metallic Ions, *J. Colloid Interface Sci.*, 2025, 138645.
18 B. H. Suryanto, Y. Wang, R. K. Hocking, W. Adamson and C. Zhao, Overall Electrochemical Splitting of Water at the Heterogeneous Interface of Nickel and Iron Oxide, *Nat. Commun.*, 2019, **10**(1), 5599.
19 M. S. S. Danish, Exploring Metal Oxides for the Hydrogen Evolution Reaction (HER) in the Field of Nanotechnology, *RSC Sustain.*, 2023, **1**(9), 2180–2196.
20 M. Bhavanari, K.-R. Lee, C.-J. Tseng, B.-J. Su, J.-M. Chen, J.-K. Chang, A. J. Bhattacharyya and C.-Y. Su, New Insights into Interface Charge-Transfer Mechanism of Copper-Iron Layered Double Hydroxide Cathodic Electrocatalyst in Alkaline Electrolysis, *J. Environ. Chem. Eng.*, 2022, **10**(2), 107287.
21 D. Alves, R. A. Moral, D. Jayakumari, E. Dempsey and C. B. Breslin, Factorial Optimization of CoCuFe-LDH/Graphene Ternary Composites as Electrocatalysts for Water Splitting, *ACS Appl. Mater. Interfaces*, 2024, **16**(38), 50846–50858, DOI: 10.1021/acsami.4c10870.
22 F. Arshad, A. Munir, A. Tahir, S. Z. Hussain, A. Jilani, A. Hussain, N. Ullah, F. Sher and I. Hussain, Microwave-Assisted Growth of Spherical Core-Shell NiFe LDH@ CuxO Nanostructures for Electrocatalytic Water Oxidation Reaction, *Int. J. Hydrogen Energy*, 2023, **48**(12), 4719–4727.
23 X. Feng, X. Hao, X. Zhao, Y. Guo, S. Ma, B. Xu, H. Liu and B. Gao, Tailoring Nanostructured NiFe-LDH Catalysts via Ammonium Fluoride-Mediated Hydrothermal Synthesis: Enhanced Electrocatalytic Performance in Oxygen Evolution Reactions, *CrystEngComm*, 2025, **27**(10), 1483–1490.
24 P. Gholami, L. Dinpazhoh, A. Khataee, A. Hassani and A. Bhatnagar, Facile Hydrothermal Synthesis of Novel Fe-Cu Layered Double Hydroxide/Biochar Nanocomposite with Enhanced Sonocatalytic Activity for Degradation of Cefazolin Sodium, *J. Hazard Mater.*, 2020, **381**, 120742.
25 W. Y. Lim and G. W. Ho, Nickel-Cobalt Layered Double Hydroxides for Photocatalytic Degradation under Visible Light Irradiation, *Procedia Eng.*, 2017, **215**, 163–170.
26 C. Xing, F. Musharavati, H. Li, E. Zalezhad, O. K. S. Hui, S. Bae and B.-Y. Cho, Synthesis, Characterization, and

Properties of Nickel–Cobalt Layered Double Hydroxide Nanostructures, *RSC Adv.*, 2017, **7**(62), 38945–38950, DOI: 10.1039/C7RA06670H.

27 A. R. Nallayagari, E. Sgreccia, L. Pasquini, M. Sette, P. Knauth and M. L. Di Vona, Impact of Anion Exchange Ionomers on the Electrocatalytic Performance for the Oxygen Reduction Reaction of B-N Co-Doped Carbon Quantum Dots on Activated Carbon, *ACS Appl. Mater. Interfaces*, 2022, **14**(41), 46537–46547, DOI: 10.1021/acsami.2c11802.

28 A. R. Nallayagari, E. Sgreccia, L. Pasquini, F. Vacandio, S. Kaciulis, M. L. Di Vona and P. Knauth, Catalytic Electrodes for the Oxygen Reduction Reaction Based on Co-Doped (BN, Si-N, SN) Carbon Quantum Dots and Anion Exchange Ionomer, *Electrochim. Acta*, 2022, **427**, 140861.

29 X. Meng, X. Liu, D. Zeng, Y. Huang, H. Wang, Z. Li and C. Yu, Recent Advances in Biomass-Derived Hydrochar for Photocatalytic and Electrocatalytic Applications, *Chem. Eng. Sci.*, 2025, 121435.

30 A. Marrocchi, E. Cerza, S. Chandrasekaran, E. Sgreccia, S. Kaciulis, L. Vaccaro, S. Syahputra, F. Vacandio, P. Knauth and M. L. Di Vona, Hydrochar from Pine Needles as a Green Alternative for Catalytic Electrodes in Energy Applications, *Molecules*, 2024, **29**(14), 3286.

31 S. Chandrasekaran, R. Narducci, E. Sgreccia, A. Haider, L. Pasquini, A. Marocchi, E. Cerza, M. L. Di Vona and P. Knauth, Sustainable Electrodes Based on Biomass-Derived Catalysts and Ionomers for the Oxygen Reduction Reaction, *J. Mater. Sci.: Mater. Energy*, 2025, **1**, 7.

32 R.-A. Becerra-Arciniegas, R. Narducci, G. Ercolani, E. Sgreccia, L. Pasquini, M. L. Di Vona and P. Knauth, Model Long Side-Chain PPO-Based Anion Exchange Ionomers: Properties and Alkaline Stability, *J. Phys. Chem. C*, 2020, **124**(2), 1309–1316, DOI: 10.1021/acs.jpcc.9b10480.

33 K. Kordek, L. Jiang, K. Fan, Z. Zhu, L. Xu, M. Al-Mamun, Y. Dou, S. Chen, P. Liu, H. Yin, P. Rutkowski and H. Zhao, Two-Step Activated Carbon Cloth with Oxygen-Rich Functional Groups as a High-Performance Additive-Free Air Electrode for Flexible Zinc–Air Batteries, *Adv. Energy Mater.*, 2019, **9**(4), 1802936, DOI: 10.1002/aenm.201802936.

34 J. Rouquerol, F. Rouquerol, P. Llewellyn, G. Maurinand K. Sing, in. *Adsorption by Powders and Porous Solids: Principles, Methodology and Applications*, Academic press, 2013.

35 S. Sun, Y. He, T. Chen, C. Sun and C. Wu, Morphology Regulated Synthesis of NiFe-Layered Double Hydroxide Nanostructures on Nickel Foam toward Efficient Oxygen Evolution Reaction, *J. Alloys Compd.*, 2023, **963**, 171304.

36 M. Shabanian, M. Hajibeygi, A. Raeisi, FTIR Characterization of Layered Double Hydroxides and Modified Layered Double Hydroxides. In *Layered Double Hydroxide Polymer Nanocomposites*, Elsevier, 2020, pp 77–101.

37 K. Nejati, S. Davary and M. Saati, Study of 2, 4-Dichlorophenoxyacetic Acid (2, 4-D) Removal by Cu-Fe-Layered Double Hydroxide from Aqueous Solution, *Appl. Surf. Sci.*, 2013, **280**, 67–73.

38 R. Khoshbouy, F. Takahashi and K. Yoshikawa, Preparation of High Surface Area Sludge-Based Activated Hydrochar via Hydrothermal Carbonization and Application in the Removal of Basic Dye, *Environ. Res.*, 2019, **175**, 457–467.

39 S. Anantharaj, K. Karthick, M. Venkatesh, T. V. Simha, A. S. Salunke, L. Ma, H. Liang and S. Kundu, Enhancing Electrocatalytic Total Water Splitting at Few Layer Pt-NiFe Layered Double Hydroxide Interfaces, *Nano Energy*, 2017, **39**, 30–43.

40 S. M. Gateman, O. Gharbi, H. G. De Melo, K. Ngo, M. Turmine and V. Vivier, On the Use of a Constant Phase Element (CPE) in Electrochemistry, *Curr. Opin. Electrochem.*, 2022, **36**, 101133.

41 Z. Xie, W. Qu, E. A. Fisher, J. Fahlman, K. Asazawa, T. Hayashi, H. Shirataki and H. Murase, Capacitance Determination for the Evaluation of Electrochemically Active Surface Area in a Catalyst Layer of NiFe-Layered Double Hydroxides for Anion Exchange Membrane Water Electrolyser, *Materials*, 2024, **17**(3), 556.

42 F. Dionigi, Z. Zeng, I. Sinev, T. M. S. Deshpande, M. B. Lopez, S. Kunze, I. Zegkinoglou, H. Sarodnik, D. Fan, A. Bergmann, *et al.*, In-situ structure and catalytic mechanism of NiFe and CoFe layered double hydroxides during oxygen evolution, *Nat. Commun.*, 2020, **11**, 2522.

43 G.-F. Li, D. Yang and P.-Y. Abel Chuang, Defining Nafion Ionomer Roles for Enhancing Alkaline Oxygen Evolution Electrocatalysis, *ACS Catal.*, 2018, **8**(12), 11688–11698, DOI: 10.1021/acscatal.8b02217.

44 P. Mardle, B. Chen and S. Holdcroft, Opportunities of Ionomer Development for Anion-Exchange Membrane Water Electrolysis: Focus Review, *ACS Energy Lett.*, 2023, **8**(8), 3330–3342, DOI: 10.1021/acsenergylett.3c01040.

45 M. K. Cho, H.-Y. Park, H. J. Lee, H.-J. Kim, A. Lim, D. Henkensmeier, S. J. Yoo, J. Y. Kim, S. Y. Lee and H. S. Park, Alkaline Anion Exchange Membrane Water Electrolysis: Effects of Electrolyte Feed Method and Electrode Binder Content, *J. Power Sources*, 2018, **382**, 22–29.

46 S. Wang, F. Yuan, G. Yang, S. Luo, M. Chen, T. Fan and J. Ma, In Situ Construction of CoFe-LDH by Regulating the Co/Fe Molar Ratio for Promoting Oxygen Evolution Reaction, *Mol. Catal.*, 2022, **525**, 112339.

47 Y. Yang, Y. Wu, D. Guo and L. Liu, Effect of Fluorine Content in Layered Double Hydroxide Catalyzing Oxygen Evolution, *Appl. Surf. Sci.*, 2024, **644**, 158810.

48 C. G. Díaz-Maroto, F. Verdugo, J. Fermoso, P. Pizarro, D. P. Serrano, I. Moreno and J. Fermoso, Hydrochars Derived from Real Organic Wastes as Carbonaceous Precursors of Activated Carbons for the Removal of NO from Contaminated Gas Streams, *Sci. Total Environ.*, 2024, **945**, 173897.

49 K.-W. Jung, S. Y. Lee, J.-W. Choi, M.-J. Hwang and W. G. Shim, Synthesis of Mg–Al Layered Double Hydroxides-Functionalized Hydrochar Composite via an in Situ One-Pot Hydrothermal Method for Arsenate and Phosphate Removal: Structural Characterization and Adsorption Performance, *Chem. Eng. J.*, 2021, **420**, 129775.

50 S. Yadav, A. Ahmad, C. Gulati, M. M. Ghangrekar and B. K. Dubey, Zn-Al@ LDH Infused Hydrochar as Cathode Catalyst for Upgrading Tetracycline Degradation and Hospital Wastewater Treatment: A Synergy of Fenton-like and Bio-Electrochemical Systems, *J. Environ. Chem. Eng.*, 2024, **12**(5), 113874.

51 W. Zou, W. Guo, X. Liu, Y. Luo, Q. Ye, X. Xu and F. Wang, Anion Exchange of Ni–Co Layered Double Hydroxide (LDH) Nanoarrays for a High-Capacitance Supercapacitor Electrode: A Comparison of Alkali Anion Exchange and Sulfuration, *Chem. Eur. J.*, 2018, **24**(72), 19309–19316, DOI: 10.1002/chem.201804218.

52 Y. Wang, Y. Liu, Z. Chen, M. Zhang, B. Liu, Z. Xu and K. Yan, In Situ Growth of Hydrophilic Nickel-Cobalt Layered Double Hydroxides Nanosheets on Biomass Waste-Derived Porous Carbon for High-Performance Hybrid Supercapacitors, *Green Chem. Eng.*, 2022, **3**(1), 55–63.

53 L. Zhang, C. Han, Z. Ye, D. Cui, J. Yang, H. Xu, H. Song, Z. Guo, X. Wu and Y. Zhao, Mo-Doped CoFe-Layered Double Hydroxides as an Efficient Bifunctional Electrocatalyst for Overall Water Splitting: Effects of Different Molybdenum Additions on Catalytic Performance, *Int. J. Hydrogen Energy*, 2024, **93**, 355–363.

54 A. Chaudhari, M. R. Kandel, A. Ali, D. R. Paudel, B. Dahal and S. Subedi, Ni-Doped Co-Layered Double Hydroxides as High-Performance Electrocatalyst for the Hydrogen Evolution Reaction, *J. Nepal Chem. Soc.*, 2025, **45**(1), 66–75.

55 H. S. Jadhav, A. Roy, B. Z. Desalegan and J. G. Seo, An Advanced and Highly Efficient Ce Assisted NiFe-LDH Electrocatalyst for Overall Water Splitting, *Sustain. Energy Fuels*, 2020, **4**(1), 312–323.

56 T. Shinagawa, A. T. Garcia-Esparza and K. Takanabe, Insight on Tafel Slopes from a Microkinetic Analysis of Aqueous Electrocatalysis for Energy Conversion, *Sci. Rep.*, 2015, **5**(1), 13801.

57 H. Prats and K. Chan, The Determination of the HOR/HER Reaction Mechanism from Experimental Kinetic Data, *Phys. Chem. Chem. Phys.*, 2021, **23**(48), 27150–27158.

58 S. Anantharaj, S. Noda, V. R. Jothi, S. Yi, M. Driess and P. W. Menezes, Strategies and Perspectives to Catch the Missing Pieces in Energy-Efficient Hydrogen Evolution Reaction in Alkaline Media, *Angew. Chem., Int. Ed.*, 2021, **60**(35), 18981–19006, DOI: 10.1002/anie.202015738.

59 R. B. Patil, M. Kaur, S. D. House, L. Kavalsky, K. Hu, S. Zhong, D. Krishnamurthy, V. Viswanathan, J. Yang and Y. Yan, Reversible Alkaline Hydrogen Evolution and Oxidation Reactions Using Ni–Mo Catalysts Supported on Carbon, *Energy Adv.*, 2023, **2**(9), 1500–1511.

60 P. J. Rheinländer, J. Herranz, J. Durst and H. A. Gasteiger, Kinetics of the Hydrogen Oxidation/Evolution Reaction on Polycrystalline Platinum in Alkaline Electrolyte Reaction Order with Respect to Hydrogen Pressure, *J. Electrochem. Soc.*, 2014, **161**(14), F1448.

61 W. Sheng, Z. Zhuang, M. Gao, J. Zheng, J. G. Chen and Y. Yan, Correlating Hydrogen Oxidation and Evolution Activity on Platinum at Different pH with Measured Hydrogen Binding Energy, *Nat. Commun.*, 2015, **6**(1), 5848.

62 R.-B. Lin and S.-M. Shih, Effects of Mass Transfer on Kinetics of Hydrogen Oxidation Reaction at Nafion/Pt-Black Thin-Film Electrodes, *J. Taiwan Inst. Chem. Eng.*, 2013, **44**(3), 393–401.

63 F. B. Spingler, A. Phillips, T. Schuler, M. C. Tucker and A. Z. Weber, Investigating Fuel-Cell Transport Limitations Using Hydrogen Limiting Current, *Int. J. Hydrogen Energy*, 2017, **42**(19), 13960–13969.

64 X. Zhao, X. Li, L. An, K. Iputera, J. Zhu, P. Gao, R.-S. Liu, Z. Peng, J. Yang and D. Wang, Nitrogen-Inserted Nickel Nanosheets with Controlled Orbital Hybridization and Strain Fields for Boosted Hydrogen Oxidation in Alkaline Electrolytes, *Energy Environ. Sci.*, 2022, **15**(3), 1234–1242.